JOURNAL OF SOLID STATE CHEMISTRY **124,** 132–142 (1996)
ARTICLE NO. 0216

The Structure of a Metastable Au–Sn Phase Determined by Convergent Beam Electron Diffraction

P. A. Midgley,[1] M. E. Sleight, and R. Vincent

H. H. Wills Physics Laboratory, University of Bristol, Tyndall Avenue, Bristol, BS8 1TL United Kingdom

Received January 3, 1996; accepted March 11, 1996

The structure of a new metastable Au–Sn phase was determined by convergent beam electron diffraction. Micrometer-sized crystals were grown by heating a metal/oxide/metal trilayer and allowing the metals to react. The new phase was tetragonal with space group *P*4/*nbm*, lattice parameters $a = 6.63(3)$ Å and $c = 5.92(3)$ Å, and composition $AuSn_4$. The phase was found to be isostructural with $PtPb_4$ with Au atoms located at 2(*a*) sites and Sn atoms at 8(*m*) sites. Conditional Patterson transforms parallel to the *c*-axis were calculated from the quasi-kinematic intensities of first-order Laue zone (FOLZ) reflections diffracted from Bloch states localized on the Sn atom strings. The contour maps showed clear peaks from Au–Sn and Sn–Sn interatomic vectors. A least-squares refinement using the FOLZ reflections gave the Sn atomic parameters as $x = 0.167(1)$, $z = 0.25(4)$.

1. INTRODUCTION

The use of convergent beam electron diffraction (CBED) patterns to determine the space group of submicrometer crystals is now a well-established and routine procedure (1). However, to go further and locate the atom positions within an unknown structure using electron diffraction is still fraught with many difficulties.

The basic limitation is the strongly dynamical nature of electron diffraction so that, in general, even from moderately thin crystals, the intensities of low order reflections quickly move away from their kinematic values. For thin organic crystals and layered inorganic materials containing principally light elements, the restrictions produced by dynamical coupling between reflections are less severe, and considerable progress has been made (2). As an alternative, the crystal structure can be imaged directly and significant advances have been made in new imaging techniques such as side-band holography (3) and through-focal series (4). Unfortunately, the resolution attained by such techniques, although nearing 1 Å, is still insufficient to solve all but the simplest of structures.

A third route, adopted by one of the authors some years ago (5), is to use the intensities of excess lines in high-order Laue zone (HOLZ) reflections which can be treated in a quasi-kinematic fashion. In general, in order to interpret the structure of the excess lines effectively, one must have a good idea of the basic structure. However, a recent publication (6) has shown how even if the structure is completely unknown, useful information can be inferred from Patterson transforms using the HOLZ intensities to enable a partial structure determination.

Last, a new scanning system has been developed by the authors (7) in which the beam is rocked at a constant angle around a zone axis and then de-rocked below the specimen to produce ''precession patterns,'' analogous to X-ray precession patterns. Using this technique, the diffracted intensities are determined by integration through the Bragg condition and are thus less prone to nonsystematic dynamical interactions. The precessed intensities are collected on a single negative and may be analyzed by standard X-ray methods without any prior knowledge of the crystal structure (8).

Reports of a possible new Au–Sn phase (9) prompted a study of this system by electron diffraction. A preliminary article describing a new tetragonal Au–Sn phase was published elsewhere (10). This paper extends the original research and applies the HOLZ excess line technique to confirm, and subsequently refine, the proposed structure.

2. GROWTH OF Au–Sn FILMS

Within a high vacuum chamber, high purity (99.99%) Sn was evaporated from a molybdenum boat onto freshly cleaved rock salt held at room temperature to form a discontinuous, but connected, polycrystalline film, typically 500 Å in thickness. The film was then exposed to air to form a thin oxide layer. Under a high vacuum, Au was then evaporated directly onto the oxide layer. By dissolving the rock salt in water, the trilayer film was transferred onto a Cu mesh grid and examined in a Philips EM430 transmission electron microscope.

The Au did not form a continuous film but was found

[1] To whom correspondence should be addressed.

0022-4596/96 $18.00

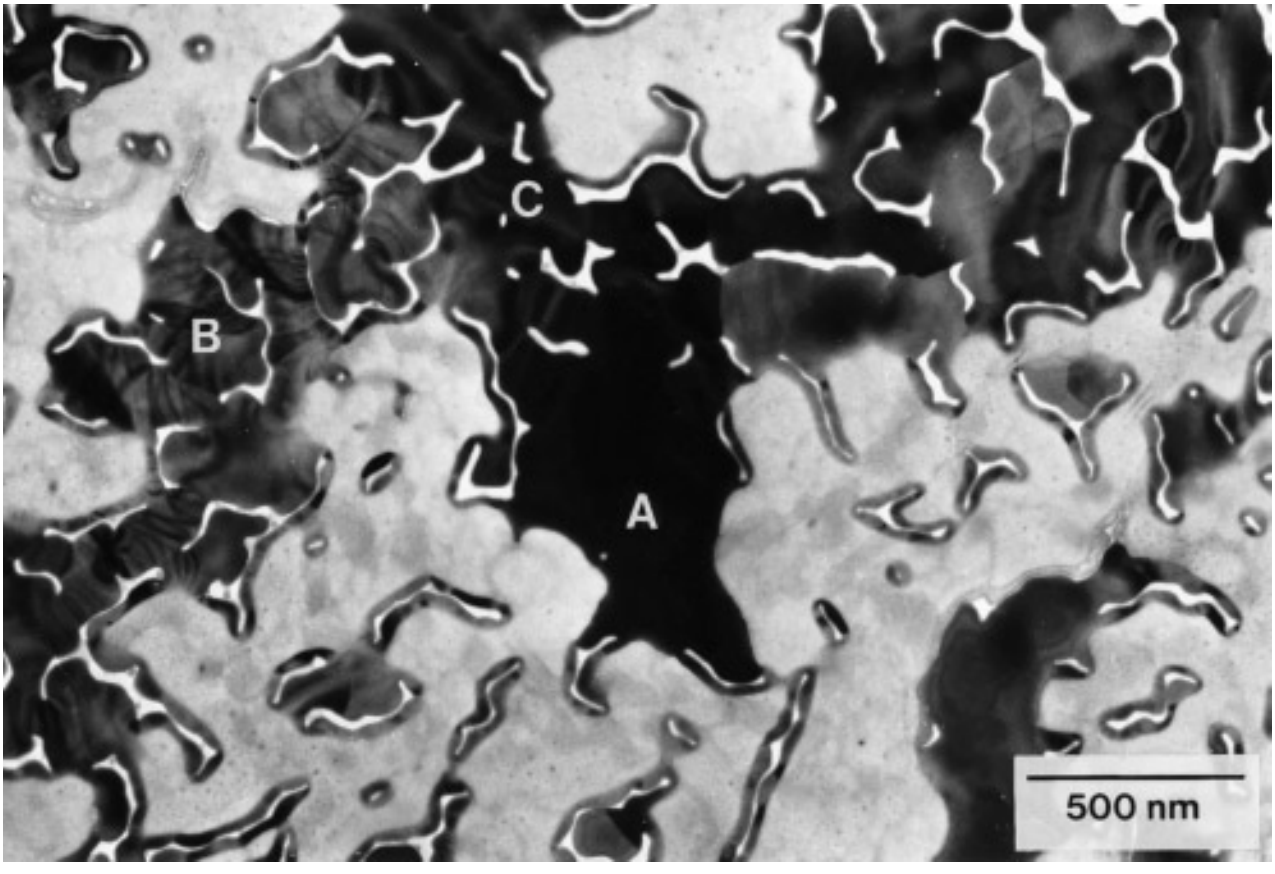

FIG. 1. Bright field image of the trilayer film after *in situ* heating, showing the τ-AuSn phase, labeled A, unreacted Sn, labeled B, the equilibrium phase AuSn, labeled C, and the underlying amorphous tin oxide.

to grow as isolated islands. The grain size of both the Au and Sn was about 0.1 μm. A preliminary examination showed that no reaction has occurred between the two metals, which were separated by a layer of tin oxide. When the films were heated *in situ* in the microscope, there was no evidence of any reaction until the temperature approached the melting point of Sn at 505 K. At these temperatures, the metals interdiffused through the oxide barrier to form several intermetallic compounds with grain sizes as large as 2 μm.

The majority of the intermetallic compounds examined were the known equilibrium phases, AuSn (space group $P6_3/mmc$) and $AuSn_2$ (*Pbca*). However, three new metastable phases were found, two with monoclinic structure and one with a tetragonal structure. It is this last phase, subsequently referred to as the τ-phase, or τ-AuSn, that is the subject of this paper.

3. RESULTS

3.1. The τ-Phase Structure

Figure 1 shows a bright field image from a typical area of the trilayer film with narrow channels separating the original Sn grains. The areas of the specimen with very weak contrast in the figure correspond to a residual film of amorphous tin oxide. Thin strips of Sn remain around the channels in the film. The area of the film showing strong bend contour contrast B, is unreacted Sn. The strongly diffracting grain labeled A in the center of the figure is the new metastable τ-phase. Just above the τ-phase is a large grain of AuSn, labeled C.

The τ-phase composition was measured from calibrated energy-dispersive X-ray spectra and was $AuSn_4$ with an estimated error of 5% in the Au : Sn ratio. To determine the space group and lattice parameters by electron diffraction, the films were transferred to a double-tilt specimen holder and cooled to 100 K to reduce thermal diffuse scattering; the metastability of these phases implies that the Debye–Waller factors were likely to be relatively large at room temperature.

Inspection of both CBED and selected area diffraction (SAD) patterns confirmed that the phase was tetragonal with a primitive Bravais lattice; unit cell parameters and c/a ratio are listed in Table 1. Figure 2a shows a [001] convergent beam pattern taken at 150 kV from the τ-phase. Figure 2b is an enlargement of a symmetry-indepen-

TABLE 1
Summary of Structural Parameters for τ-AuSn

Space group	*P*4/*nbm*		
Lattice parameters	a = 6.63(3) Å		
	c = 5.92(3) Å		
	c/a = 0.894(4)		
Structure	tP10 in Pearson notation, isostructural with $PtPb_4$		
Atom positions	x = 0.167(1)		
	z = 0.25(4)		
Bond lengths	Au–Au	4.69(2) Å	
	Au–Sn	2.9(4) Å	
	Sn–Sn (in basal plane)		3.50(3) Å
	Sn–Sn (out of basal plane)		3.3(5) Å

dent sector within the first-order Laue zone (FOLZ) showing slightly overlapping discs. The 4*mm* whole pattern symmetry was consistent only with point groups 4*mm* or 4/*mmm*. Careful inspection of the pattern revealed that the FOLZ contains twice as many reflections as the zero layer. This was attributed to the presence of a diagonal glide in the (001) basal plane. The point group was therefore 4/*mmm*. In addition the observation of dark bars, or Gjønnes–Moodie lines of absence (11) in FOLZ reflections of type 0k1, where k is odd, indicated a b-glide on the {100} planes. These glide planes were confirmed by tilting about a ⟨100⟩ axis to a pattern such as Fig. 3, where Gjønnes–Moodie lines were visible in reflections of type 0kl (k odd). The space group was therefore *P*4/*nbm*. It was noted that all the τ-phase grains studied showed a strong texture with the **c**-axis normal to the film plane.

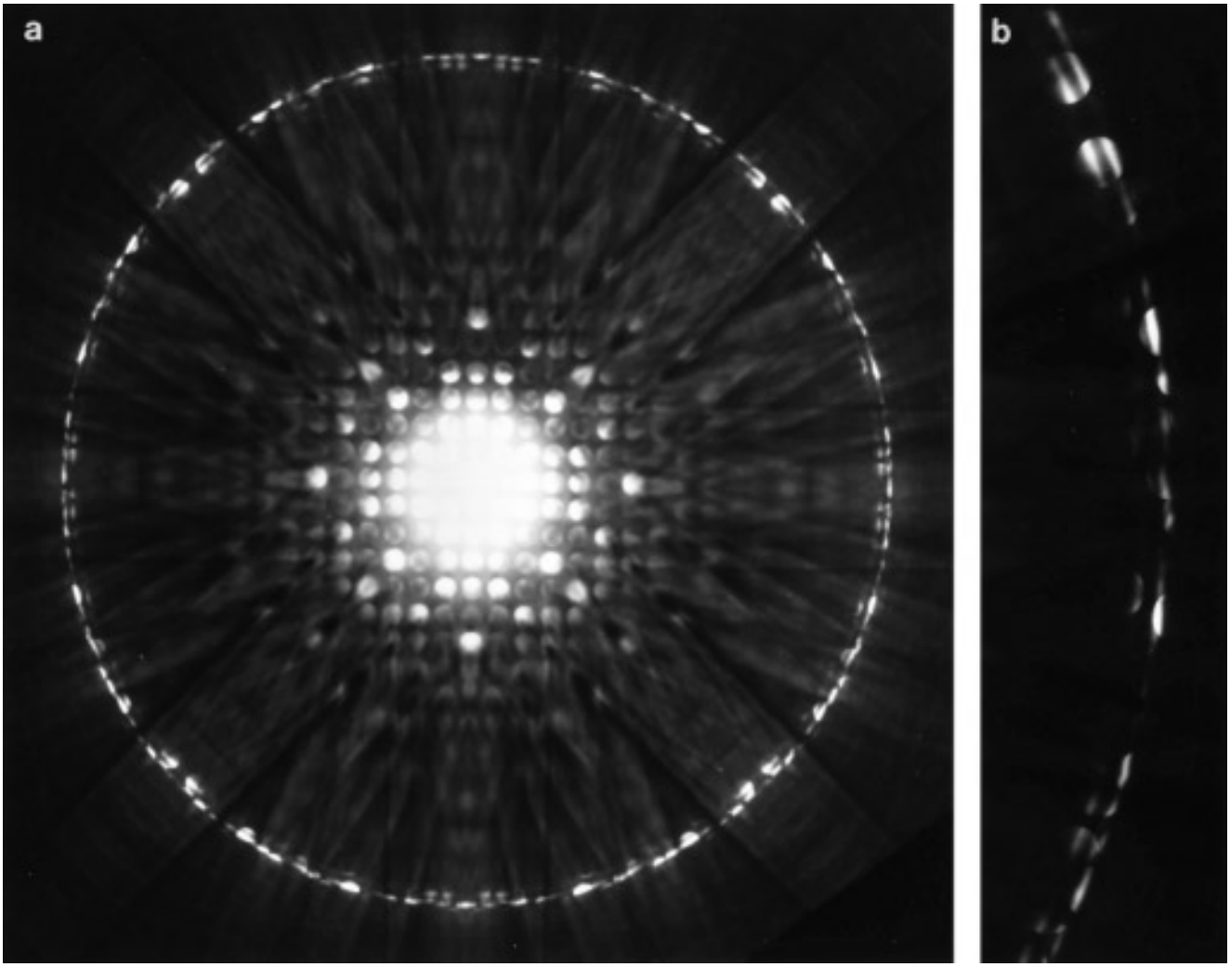

FIG. 2. (a) Convergent-beam electron diffraction pattern recorded at 150 kV parallel to the [001] zone axis of the τ-AuSn phase at 150 kV. The whole pattern has 4*mm* symmetry. The n-glide in the basal plane of the structure is confirmed by the doubling of reflections in the FOLZ ring compared to the zero layer. (b) Enlargement of a symmetry-independent section of the FOLZ ring, showing two excess lines (branches) within the disks. The FOLZ disks are slightly overlapping.

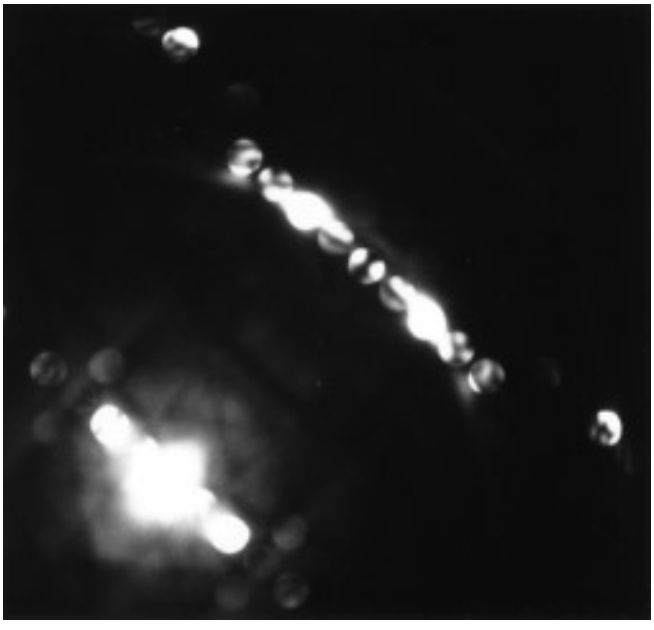

FIG. 3. CBED pattern taken near the [001] zone axis, tilted about the ⟨100⟩ direction. A Gjønnes–Moodie line of absence (dark bar) can be seen in the reflection of type 0*k*l (*k* odd), in the center of the Kikuchi band, indicating a *b*-glide on the {100} planes.

The τ-phase lattice parameters, space group, and composition listed in Table 1 were not consistent with any of the equilibrium or metastable Au–Sn phases listed in the literature (12). At this stage, it became apparent that the phase was likely to be isostructural with $PtPb_4$ (13). However, the analysis was continued to confirm the structure and to determine the atomic parameters from CBED patterns.

3.2. HOLZ Diffraction

The approach to structure determination and refinement is based on the method established by one of the authors using HOLZ intensities (5). In the kinematic limit, the effective potential controlling the amplitudes of HOLZ reflections in the *n*th layer of the reciprocal lattice perpendicular to the **c**-axis is given by the conditional projected potential $U^n(\mathbf{R})$ defined as

$$U^n(\mathbf{R}) = \int_0^1 U(\mathbf{r}) \exp(-2\pi i n z)\, dz, \qquad [1]$$

where **R** is a 2-D position vector within the projected cell, z is a fractional coordinate parallel to **c** and $U(\mathbf{r})$ represents the conventional 3-D crystal potential in standard form.

By substituting into Eq. [1] an expansion of $U(\mathbf{r})$ as a Fourier sum over U_g's an equivalent expression for $U^n(\mathbf{r})$ is obtained

$$U^n(\mathbf{R}) = \sum_{\mathbf{G}_n} U_{\mathbf{G}_n} \exp(2\pi i \mathbf{G}_n \cdot \mathbf{R}), \qquad [2]$$

where $\mathbf{G}_n$ is a 2-D vector within the *n*th layer of the reciprocal lattice normal to **c**. Equation [2] is a 2-D Fourier sum over the U_g coefficients restricted to the *n*th layer; for $n = 0$, Eqs. [1] and [2] reduce to the usual definitions of the projected potential $U^0(\mathbf{R})$. The higher order conditional potentials are generally complex because a phase factor $\exp(-2\pi i n z)$ is attached to the potential integrated along z. For example, the contribution to $U^1(\mathbf{R})$ by a single atom at height $z = \frac{1}{4}$ will be entirely negative imaginary, and that from a single atom at height $z = \frac{1}{2}$ will be negative real.

However, HOLZ reflections diffracted around a major zone axis show distinct excess lines slightly displaced from the Bragg condition. These lines correspond to diffraction out of excited Bloch states for the projected potential. At major zone axes typically only 2 or 3 states are significantly excited and thus the electron wavefunction can be adequately represented by a sum over only these excited states.

The most tightly bound branches (and also the ones most absorbed) that diffract into HOLZ excess lines generally fall inside the Bragg condition and correspond to Bloch states localized on the strongest atom strings in the projected potential. The effective conditional potential is then modified to $U^n(\mathbf{R})$ multiplied by the Bloch state amplitude $\tau^{(j)}(\mathbf{R})$ for branch j of the dispersion surface. The multiplication of a sharply localized string potential by the slowly varying function $\tau(\mathbf{R})$ implies that the shape and depth of the atom strings is modified but the positions of projected atoms are not significantly affected to a very good approximation.

For projected cells that contain sets of symmetry-related atomic strings, the excited Bloch states are generally 1*s*- or 2*s*-type states localized on the atom strings or a combination of these states to give molecular Bloch state clusters. Provided that the string potentials are well separated, the splitting between branches of the dispersion surface for the molecular states remains small, and the branch cluster can be treated as a single composite Bloch state localized on all of the symmetry-related strings (4). When multiplied by $U^n(\mathbf{R})$, the effect is to isolate a subset of symmetry-related atom strings within the conditional potential. It then follows that the HOLZ excess line amplitudes remain proportional to the corresponding partial structure factor in a quasi-kinematic limit where the crystal thickness is much less than the HOLZ extinction distances (typically $\sim 1\ \mu$m).

Knowing the approximate crystal structure, dynamical calculations give the Bloch state amplitude and excitation. HOLZ intensities can be used to confirm the structure and then refine atomic parameters to a precision approaching measurements made by X-rays.

No allowance is made for dynamic coupling between

HOLZ reflections. In practice, some reflections may show evidence of this in the form of intensity variation along the excess line. These reflections can be omitted from the refinement procedure, but their effect will be minimized overall if a large number of HOLZ reflections are used. Provided that the HOLZ reflections are high multiples of the reciprocal basis vectors, even small atomic displacements produce large changes in the associated structure factors.

3.3. Measurement of Intensities

CBED patterns centered on the [001] zone axis were recorded with a probe of size 10 nm at voltages between 150 and 270 kV in 10 kV steps. The morphology of the τ-phase grains implied that the patterns were recorded from areas somewhat thicker than ideal and this is reflected in the final analysis as large dynamical perturbations. Nevertheless, it has been shown (14) that the principal effect of 2-beam extinction within HOLZ intensities used to refine an atomic parameter is to increase the statistical uncertainty in that parameter and not to introduce any significant systematic error.

Dynamical calculations using the atom positions for the $PtPb_4$ structure were consistent with the two excess lines shown in Fig. 2, where the weaker inner line corresponded to a 1*s* state localized on the Sn atom strings (Fig. 4a) and the outer line was associated with diffraction from a hybrid combination of 2*s* states sitting on both the Au and Sn strings (Fig. 4b). The sign of each peak within the hybrid 2*s* state was found to be negative. This is important as the scattering into the a HOLZ reflection is governed by both $U^n(\mathbf{R})$ and $\tau^{(j)}(\mathbf{R})$ as discussed previously. For example, if the peaks on the Au strings within the 2*s* state were of opposite sign to those on the Sn strings this would result in the effective scattering potential for the Au being of opposite polarity to that of the Sn. Calculations revealed a third weakly excited line that was expected to lie inside the inner 1*s* Sn branch. This corresponded to a 1*s* state on the Au atom strings (Fig. 4c) but for typical thicknesses, say 500 Å, this branch is highly absorbed and therefore was not visible in the pattern.

Analysis was restricted to the outer branch because of its high visibility and also the strong azimuthal intensity variation associated with the Sn atom positions. Symmetry independent FOLZ reflections (82) were indexed from the voltage sequence. Intensities were measured on an eight-point interval scale by visual comparison with an array of calibration lines exposed on a photographic film and overlapped with the original negative, thereby avoiding local perturbations of local intensities due to nonsystematic interactions and providing a simple background subtraction. Sufficient reflections were common to pairs of negatives to give a reliable cross-calibration of intensities measured from negatives taken at different voltages and thicknesses. The intensity data for the *hk*1 reflections are plotted in Fig. 5. Absences in the data set correspond to reflections which were perturbed by strong dynamical interactions and were therefore omitted. Crosses indicate reflections kinematically forbidden by the *b*-glide in the {100} planes.

3.4. Patterson Transforms

The Patterson or self-correlation function for $U(\mathbf{r})$ is defined as

$$P(\mathbf{r}) = \frac{1}{V}\int U(\mathbf{r}')U(\mathbf{r}+\mathbf{r}')\,d\mathbf{r}', \qquad [3]$$

where V is the volume of unit cell.

Conditional projections apply equally well to Patterson transforms, where

$$P^n(\mathbf{R}) = \int_0^1 P(\mathbf{r})\exp(-2\pi i n z)\,dz \qquad [4]$$

and

$$P^n(\mathbf{R}) = \sum_{\mathbf{G_n}} |U_{\mathbf{G}_n}|^2 \exp(2\pi i \mathbf{G}_n \cdot \mathbf{R}). \qquad [5]$$

Notice that like $U^n(\mathbf{R})$, the conditional Patterson transforms $P^n(\mathbf{R})$ are generally complex due to the z-dependent phase factor in the integral.

It is often helpful to plot Patterson transforms using the $E^2 - 1$ formalism (15), where $E^2 = I/\langle I\rangle$ where I is the observed intensity and $\langle I\rangle$ is the mean observed intensity for all reflections included in the transform. This produces a Patterson function with the self-correlation peak at the origin removed. This is useful, in that vectors of small magnitude which are normally swamped by the origin peak may be revealed.

3.5. The Symmetry of the Conditional Transforms

For space group $P4/nbm$, the symmetry of the related Patterson group is $P4/mmm$ and the projection group along [001] for both $U^0(\mathbf{R})$ and $P^0(\mathbf{R})$ is $p4mm$. The two-dimensional space groups of the conditional projections are less simple because the z coordinates of the atoms are included in the transforms through the phase factor $\exp(-2\pi i n z)$. The symmetry of the conditional projections is given by the layer group (16).

Consider the symmetry of $U^n(\mathbf{R})$. The *b*-glides parallel to {100} and {110} in $P4/nbm$ (Fig. 6a) become mirrors in the real part of $U^n(\mathbf{R})$ and the layer group is $p4mm$, No. 52 in Weber notation (17), the same as the projection group for $U^0(\mathbf{R})$. In the imaginary part, however, the *b*-glides

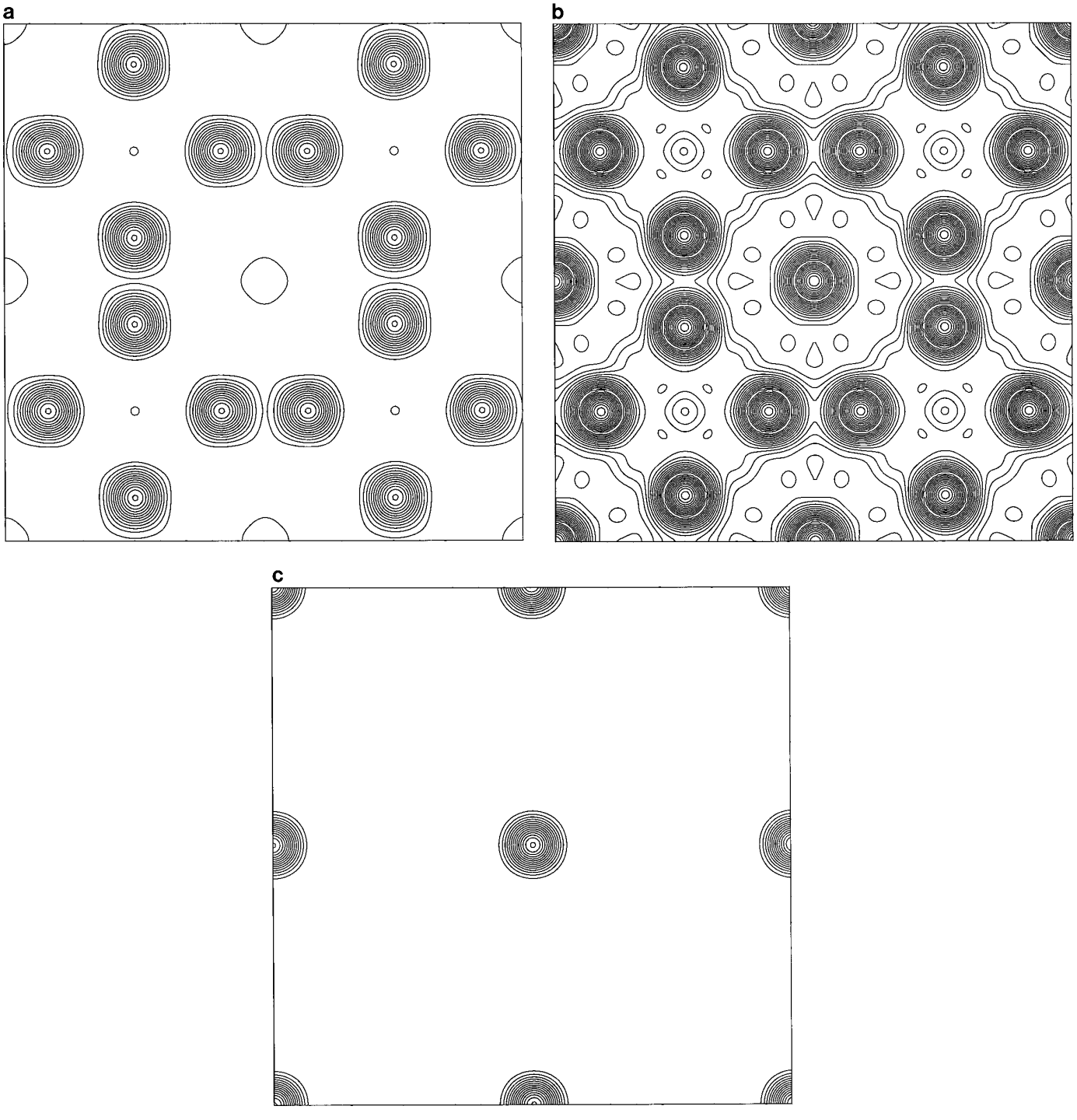

FIG. 4. The significantly excited Bloch states at the [001] zone axis of the τ-phase calculated using the $PtPb_4$ structure. Only the modulus of the Bloch state is shown and the area in each figure is equivalent to four projected unit cells. (a) shows a 1*s* state on the Sn atom strings, (b) shows a hybrid 2*s* state on both Au and Sn strings, and (c) shows the third excited state, a 1*s* state on the Au atom strings which is highly absorbed and is invisible in the CBED patterns.

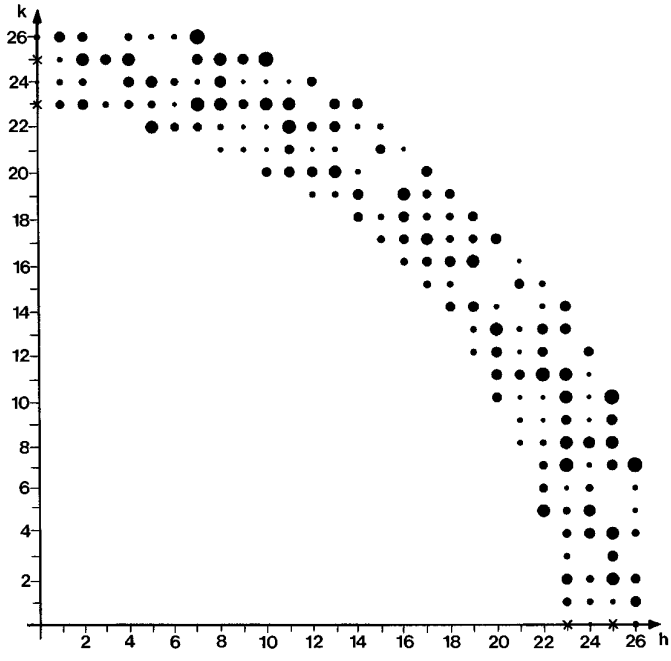

FIG. 5. Map of $hk1$ reflections used to calculate the Patterson transform $P^1(\mathbf{R})$. The radii of the circles size are proportional to the measured intensity. Reflections of type $h01$ (h odd) are forbidden by the b-glide and are shown as small crosses.

become antimirrors giving the layer group $p422$ (No. 55). If the 8(m) atoms in the $PtPb_4$ structure are at "ideal" heights of $z = \frac{1}{4}$ then $U^n(\mathbf{R})$ is pure real for n even, and the 8(m) atoms contribute only a pure imaginary component for n odd. The Patterson transform $P^n(\mathbf{R})$ is pure real for all values of z and n. The layer symmetry is again $p4mm$. These pattern symmetries are illustrated in Fig. 6 for the $PtPb_4$ structure with the x parameter on the 8(m) sites taken to be exactly $\frac{1}{6}$ for simplicity. The basic $PtPb_4$ structure is sketched in Fig. 6b and the corresponding schematic maps for $U^1(\mathbf{R})$ and $P^1(\mathbf{R})$ are shown in Fig. 6c and 6d, respectively. The peaks shaded grey correspond to four separate Au–Sn interatomic vectors, two with phase factor $\exp(-2\pi iz)$ and two with $\exp(+2\pi iz)$, giving a total multiplicative factor of $\cos(2\pi z)$. For $z = \frac{1}{4}$, these phase factors are equal in magnitude but of the opposite sign and therefore the peak will be absent in the Patterson transform.

3.6. Experimental Patterson Transforms from τ-AuSn

The Patterson transform $P^1(\mathbf{R})$ was calculated from the FOLZ intensity data (shown in Fig. 5) for comparison with the transform expected from the $PtPb_4$ structure. The experimental transform is shown in Fig. 7a. Although peaks can be distinguished from the background "ripple," it is beneficial to compare the experimental transform with an ideal transform determined from the same set of FOLZ reflections but now calculated using kinematic intensities derived from the known $PtPb_4$ structure. This is shown in Fig. 7b. Even in this ideal situation, the background ripple is large due to the limited data set used in the transform. Comparing Figs. 7a and b, it is clear that despite the errors in the experimental FOLZ intensity data, there is a substantial correlation between the two transforms, confirming that the τ-phase was isostructural with $PtPb_4$.

Inspection of the experimental transform shows only five peaks (excluding the origin peak) in the symmetry-independent octant whereas there are six in the schematic transform. The missing peak (also very weak in 7b) is associated with the Au–Sn interatomic vectors within the $p4mm$ layer group. It was stated earlier that this peak is absent if the z-coordinate of Sn is $z = \frac{1}{4}$. The z-parameter of the Pb atom in the $PtPb_4$ structure is 0.255, close to the ideal value of $\frac{1}{4}$, and therefore the peak is very weak. The absence of a peak in the experimental transform indicates that the Sn z-parameter in the τ-phase structure must also be close to the value of $\frac{1}{4}$. The peak at the center of the experimental Patterson transform is much weaker than expected. To explain why, consider the strongest reflections in the FOLZ. These will be dominated by the eight Sn atoms in the unit cell scattering in phase and will undoubtedly be prone to extinction effects, emphasised by the necessity of using relatively thick crystal. This extinction will be most evident in the peak at the center of the transform which represents the summed contribution from two Au–Au vectors minus eight Sn–Sn vectors for $z = \frac{1}{4}$. As discussed below, Au and Sn atoms scatter into almost separate subsets of FOLZ reflections, and therefore it is expected that extinction will reduce the amplitude of the Sn reflections more quickly, reducing the overall peak strength by mutual cancellation of Au and Sn contributions.

An approximate value of the x parameter can be estimated by simply measuring the peak positions on the transform. The clearest peak on the experimental pattern is that at the ($\frac{1}{2}$, y) position, indicated by the arrow. This interatomic vector is equivalent to a displacement of ($\frac{1}{2}$, $\frac{1}{2} - 2x$) in the (001) basal plane of the structure. Therefore, the y-axis position of the peak gives a direct measure of x, where $y = \frac{1}{2} - 2x$. Measurement of the peak position gave $x = 0.17(1)$.

3.7. Refinement of the Atomic Parameters

The experimental Patterson transform of Fig. 7a confirmed that the τ-phase was isostructural with the $PtPb_4$ structure, with two free parameters, x, controlling the 8(m) positions of the Sn atoms in the basal plane and estimated to be 0.17, and z, which was estimated to be 0.25 from the absence of peaks in the Patterson transform.

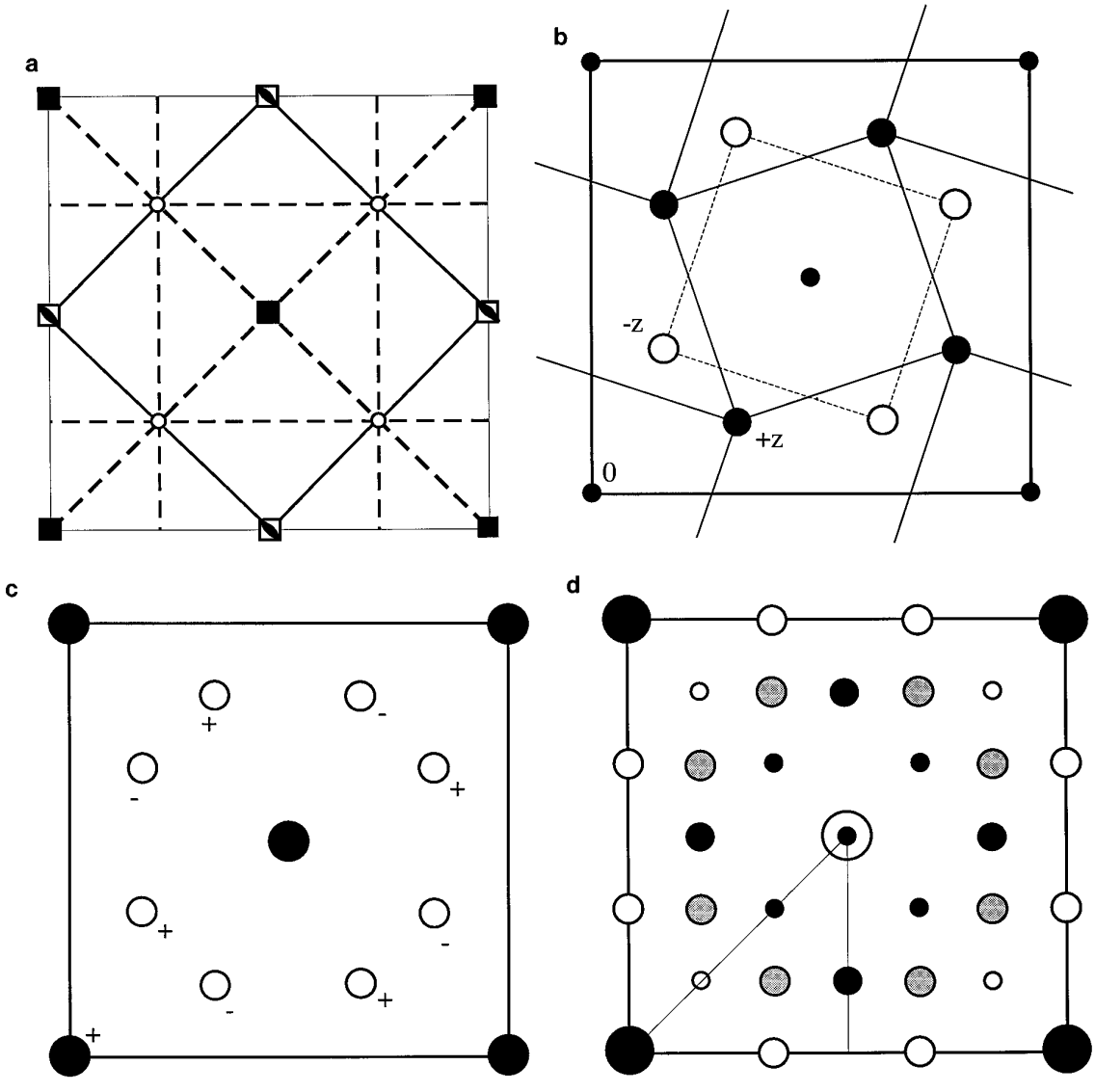

FIG. 6. (a) Schematic diagram of the rotation axes, glide planes, and mirrors parallel to **c** in $P4/nbm$ using standard notation. The projected cell area is half the size of the cell shown in the figure. (b) Diagram of the $PtPb_4$ structure where the small filled circles represent the Pt atoms at $z = 0$ and the larger filled and open circles represent Pb atoms at $+z$ and $-z$, respectively. (c) Schematic map of $U^1(\mathbf{R})$ where filled circles represent the potential on the Pt atom strings (pure real) and open circles represent the potential on the Pb atom strings. For atoms at $z = \pm 1/4$, the potential is pure imaginary and the sign of the potential is shown in the figure. (d) Schematic map of $P^1(\mathbf{R})$ where filled circles have zero phase factor, open circles represent correlation peaks multiplied by the factor $\cos 4\pi z$ (equal to -1 if $z = 1/4$) and shaded circles represent peaks multiplied by the factor $\cos 2\pi z$ (equal to zero if $z = 1/4$). The triangle corresponds to the symmetry-independent octant mentioned in the text. The radii of the circles represents the strength of the peak expected in the transform. The peak at the center is associated with both Au–Au and Sn–Sn vectors.

The x parameter was refined independently of the z parameter, which was initially fixed at $\frac{1}{4}$. The value of z was then changed to a new value and x was refined again. Although somewhat laborious, it was felt this was a much safer method of refinement, given the large uncertainties in the z parameter value, than using a global minimum search routine.

The structure factor for $hk1$ reflections can be grouped into two sets,

$$h + k = 2n$$

$$|F_{hk1}|^2 = 4f_{\mathrm{Au}}^2 + 16f_{\mathrm{Au}}f_{\mathrm{Sn}}\cos 2\pi z \cos 2\pi hx \cos 2\pi kz + 64\, f_{\mathrm{Sn}}^2 \cos^2 2\pi z \cos^2 2\pi hx \cos^2 2\pi kx \quad [6]$$

$$h + k = 2n + 1$$

$$|F_{hk1}|^2 = 64 f_{\mathrm{Sn}}^2 \sin^2 2\pi z \sin^2 2\pi hx \sin^2 2\pi kx. \quad [7]$$

For $z = \frac{1}{4}$, these expressions simplify to

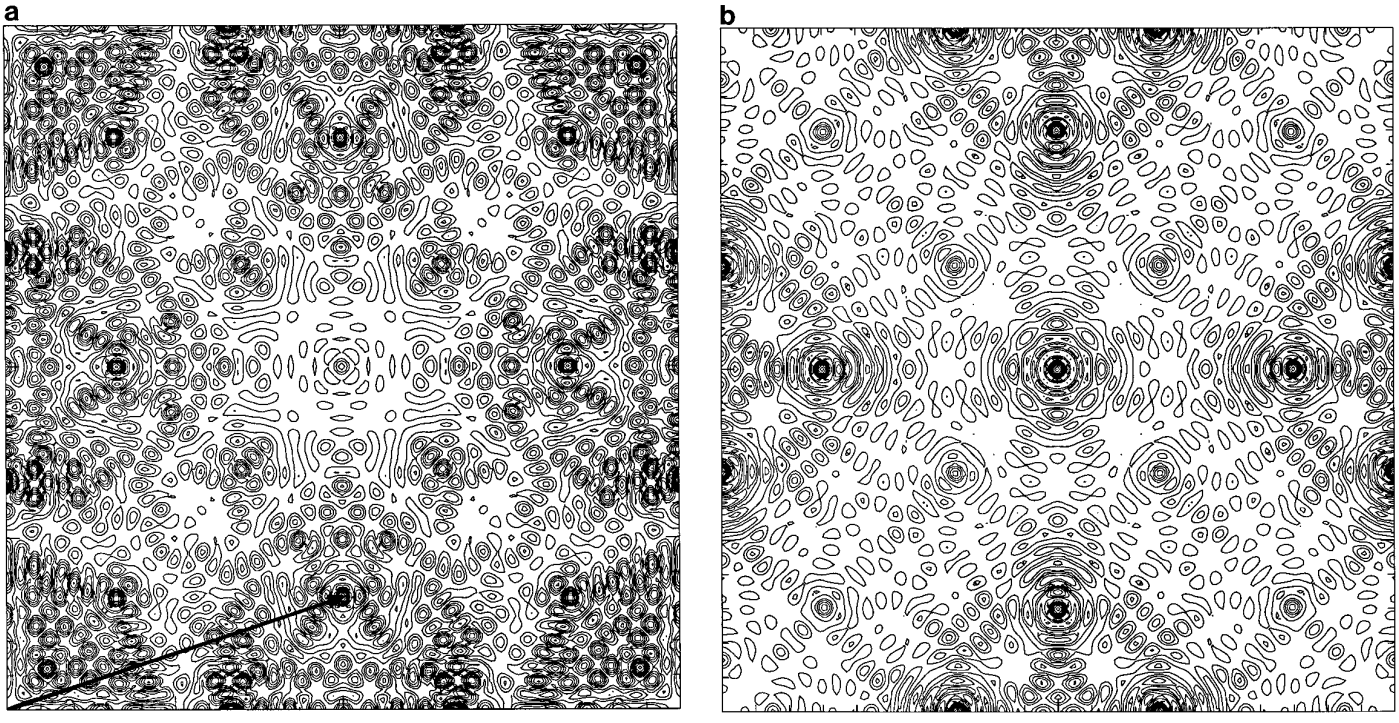

FIG. 7. (a) Experimental conditional Patterson transform $P^1(\mathbf{R})$ calculated from the data in Fig. 5; the origin peak has been removed. The arrow indicates a Sn–Sn interatomic vector. (b) Conditional Patterson transform calculated from the known $PtPb_4$ atomic parameters, for comparison to the transform shown in (a).

$$h + k = 2n \qquad |F_{hk1}|^2 = 4f_{\mathrm{Au}}^2 \qquad [8]$$

$$h + k = 2n + 1 \quad |F_{hk1}|^2 = 64f_{\mathrm{Sn}}^2 \sin^2 2\pi hx \sin^2 2\pi kx. \qquad [9]$$

Thus, in the ''ideal'' situation, with $z = \frac{1}{4}$, the reflections alternate with contributions to the intensity from either the Au atoms or the Sn atoms but not both.

Further, if the ''doubly ideal'' situation is reached with $x = \frac{1}{6}$ and $z = \frac{1}{4}$, then

$$|F_{hkl}|^2 = 0 \quad \text{if } h + k = 2n + 1, \quad \text{and } h \text{ or } k = 3n.$$

The estimated values of x and z for the τ-phase are close to this doubly ideal situation and thus one would expect every 3rd row of Fig. 5 to be weak. Allowing for dynamical perturbations and measurement error then this patterning can indeed be seen in the figure.

The refinement procedure was based on a least-squares method (5) to minimize E, defined as the root-mean square difference between the observed and calculated intensities (I_0 and I_c, respectively) for N symmetry-independent reflections, where

$$E(x) = \sqrt{\frac{\Sigma\,(I_0 - KI_c(x))^2}{N}} \qquad [10]$$

and the calculated intensities were normalized to the experimental data using $K = \Sigma I_0 I_c / \Sigma I_c^2$. An estimate for the standard deviation in x was obtained from the width of the minimum in the function $E(x)$ as described in the Appendix of (4). In Fig. 8a the function $E(x)$ is plotted for x in the range from 0.1 to 0.2, with z fixed at 0.25. A clear minimum is obtained for $x = 0.167$ with a standard deviation of 0.001.

The z parameter was then varied keeping x constant to determine the function $E(z)$ and obtain an estimate of the error for the value of z quoted. This is shown in Fig. 8b. The z parameter was found to be 0.25 ± 0.04. The broad minimum in the function $E(z)$ is reflected in the large error for z. This size of error is not unexpected as the intensity data will be very insensitive to changes in the c-axis direction, parallel to the beam.

A Debye–Waller factor was included in the refinement although this had little effect on the position of the minimum. The value of the Debye–Waller factor obtained cannot be relied upon in refinements using HOLZ data collected this way. Often, the best refinement is obtained for a negative Debye–Waller factor (7) as was the case here ($B = -0.11$ Å^2), but this is of course physically meaningless. The negative value for B can be explained by the use of a simple visual comparison when measuring the FOLZ intensities. The eye appears to automatically compensate

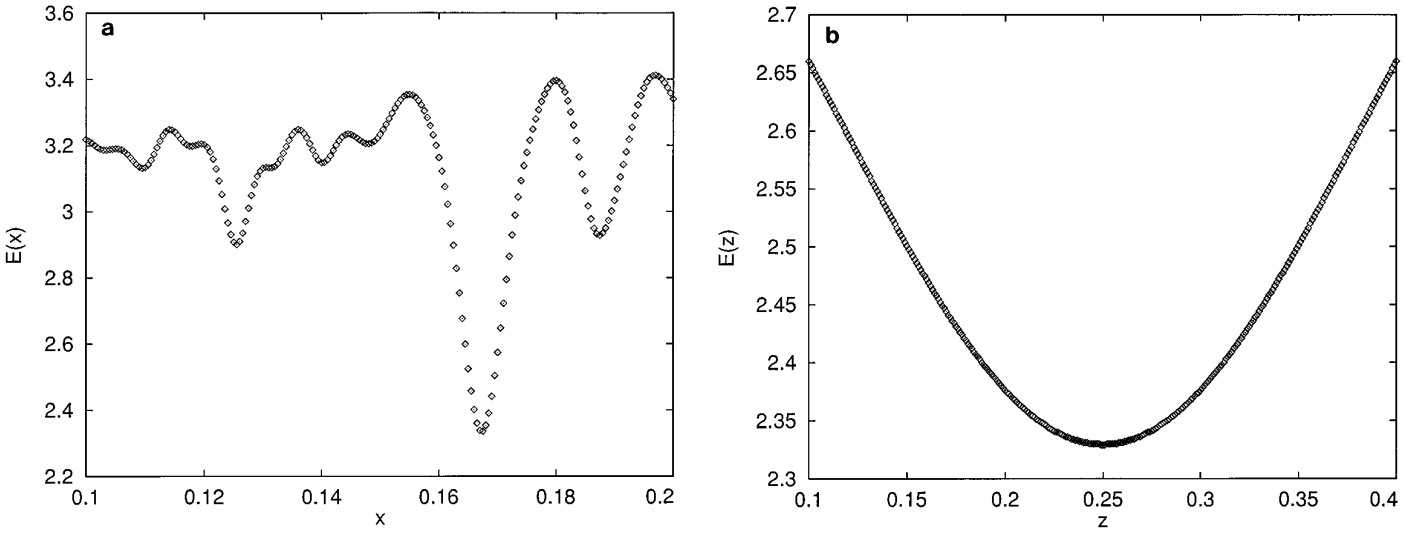

FIG. 8. (a and b) Variation of E (see Eq. [10]) with atomic parameters x and z, respectively, calculated from the observed FOLZ intensities. Minima are found for $x = 0.167(1)$ and $z = 0.25(4)$.

for the reduction in overall intensity with increasing scattering angle and therefore increases the intensity of reflections at higher values of g relative to those at lower values. Calibration of intensities between negatives then gives rise to an over-compensation for reflections of high order and therefore, in the refinement, leads to a reduction in the Debye–Waller factor, even to a negative value.

A reliability factor, or R factor, defined as $R = \Sigma|I_0 - I_c|/\Sigma I_0$ was determined using the refined intensities and gave a value of $R = 0.49$ at $x = 0.167$. Although this figure is large compared to most X-ray refinements, due mainly to dynamical perturbations, the error in the refined value of x remained small because of the large number of high-order reflections in the data set.

4. DISCUSSION OF THE τ-AuSn STRUCTURE

Crystallographic data for τ-AuSn are summarized in Table 1. In the structure, sets of Sn atoms at $z \approx \frac{1}{4}, \frac{3}{4}$ are arranged antisymmetrically with respect to each other. The squares of these nets are centered by Au atoms at $z = 0$ to form square antiprisms. The Au and Sn nets form a unit of 3 layers which is well separated from the adjacent 3-layer unit. The Au–Sn bond length along the edge of the prism is 2.9(4) Å. The Sn–Sn bond length within the basal plane is 3.50(3) Å.

Alternatively, the structure can be described as illustrated in Fig. 9, to emphasize the importance of the Sn–Sn bonding. The Sn atoms lie within two sets of orthogonal planes containing hexagonal nets parallel to (110) and $(1\bar{1}0)$ planes. These sets of hexagons are fully locked into a Kagomé-like net. For clarity, only the Sn atoms within a single plane are shown in Fig. 9. Similar nets orthogonal to the plane of the paper would run along the $\langle 1\bar{1}0\rangle$ directions every $\frac{1}{2}$ unit cell.

Th hexagons are regular if $c/a = (\frac{2}{3})^{1/3} \approx 0.817$ and $x = \frac{1}{6}$. In the τ-phase, c/a is much larger and therefore, as shown in Fig. 9, the hexagons are elongated in the **c**-axis direction. The two Sn–Sn bond lengths quoted in the table represent the two independent edge lengths for the hexagonal nets. The τ-AuSn phase is the only phase known to the authors to be isostructural with $PtPb_4$.

5. CONCLUSIONS

A trilayer of tin/tin oxide/gold was grown by thermal evaporation. The two metals were heated *in situ* in a TEM

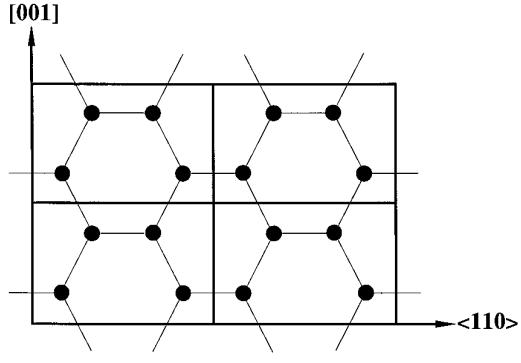

FIG. 9. A slice through the τ-phase structure emphasising the arrangement of Sn atoms in a Kagomé-like net parallel to the {110} planes. Four projected unit cells are shown for clarity.

and reacted to form novel intermetallic phases. The complex multiphase nature of the sample prohibited conventional X-ray techniques and, so analysis was carried out by electron diffraction.

One of the new phases was found to be tetragonal, space group $P4/nbm$, lattice parameters $a = 6.63(3)$ Å, $c = 5.92(3)$ Å, with a composition $AuSn_4$. The new phase was thought likely to be isostructural with $PtPb_4$ and convergent beam diffraction techniques were used to confirm this and subsequently refine the atom positions.

The intensity of excess lines in FOLZ reflections were used to generate a conditional Patterson transform. The positions of peaks within the transform, relating to interatomic vectors within the structure, could be identified above the background ripple resulting from Fourier series truncation and measurement error. The relative strengths of the peaks were affected by dynamical scattering caused by using a crystal of thickness larger than the ideal kinematic limit. Interpretation of the conditional transforms was aided by comparison with ideal transforms from the isostructure $PtPb_4$. The basal plane atomic parameter of Sn was then refined to an accuracy comparable to X-ray methods and an estimate was given for the Sn z parameter.

The new phase was closely related to the equilibrium, orthorhombic $AuSn_4$ phase. The equilibrium phase can be recovered by shifting the second layer of Sn atoms by $\frac{1}{2}$ unit cell, with respect to the first layer, in the **a** direction. These shifts in the structure lead to a small orthorhombic distortion and a concurrent doubling of the c-axis lattice parameter.

ACKNOWLEDGMENTS

One of the authors (P.A.M.) acknowledges support from a Royal Society Research Fellowship and another (M.E.S.) acknowledges the EPSRC and ICI for the award of a CASE studentship.

REFERENCES

1. J. W. Steeds and R. Vincent, *J. Appl. Crystallogr.* **16,** 317 (1983).
2. J. M. Cowley, *Prog. Mater. Sci.* **13,** 267 (1965); B. K. Vainstein, B. B. Zvyagin, and A. S. Avilov, *in* "Electron Diffraction Techniques" (J. M. Cowley, Ed.), Vol. 1, pp. 216–312. Int. Union Crystallogr. and Oxford Univ. Press, London, 1992; D. L. Dorset, *Ultramicroscopy* **45,** 5 (1992).
3. H. Lichte, *Ultramicroscopy* **47,** 223 (1992).
4. W. Coene, G. Janssen, M. Op de Beeck, and D. Van Dyck, *Phys. Rev. Lett.* **69,** 37 (1992).
5. R. Vincent, D. M. Bird, and J. W. Steeds, *Phil. Mag. A* **50,** 745 (1984).
6. R. Vincent and D. R. Exelby, *Acta Crystallogr. A* **51,** 801 (1995).
7. R. Vincent, and P. A. Midgley, *Ultramicroscopy* **53,** 271 (1994).
8. P. A. Midgley, M. E. Sleight, and R. Vincent, "Int. Conf. Elec. Microsc., Paris," p. 919 (Les Editions de Physique, Les Ulis). 1994.
9. D. C. Dufner and L. Eyring, *J. Solid State Chem.* **62,** 112 (1986).
10. P. A. Midgley, M. E. Sleight, and R. Vincent, "Int. Conf. Elec. Microsc., Paris," p. 873 (Les Editions de Physique, Les Ulis). 1994.
11. J. Gjønnes and A. F. Moodie, *Acta. Crystallogr.* **19,** 65 (1965).
12. P. Villars and L. D. Calvert, "Pearson's Handbook of Crystallographic Data for Intermetallic Phases." American Society for Metals, Ohio, 1985.
13. U. Rösler and K. Schubert, *Naturwissenschaften* **58,** 331 (1951).
14. R. Vincent and D. R. Exelby, *Phil. Mag. B* **68,** 513 (1993).
15. G. H. Stout and L. H. Jensen, "X-Ray Structure Determination; A Practical Guide." Wiley, New York, 1989.
16. A. V. Shubnikov and V. A. Koptsik, "Symmetry in Science and Art." Plenum Press, New York, 1974.
17. D. R. Exelby, Ph.D. thesis, University of Bristol, 1991.